This article has been accepted for publication in IEEE/OSA Journal of Lightwave Technology. This is the author's version which has not been fully edited and content may change prior to final publication. Citation information: DOI 10.1109/JLT.2022.3222131
Accepted Manuscript
Version of record at: https://doi.org/10.1109/JLT.2022.3222131

Fully Automatic In-Situ Reconfiguration of Optical Filters in a CMOS-Compatible Silicon Photonic Process

Md Jubayer Shawon, *Student Member, IEEE,* and Vishal Saxena, *Senior Member, IEEE*

***Abstract*—Automatic reconfiguration of optical filters is the key to novel flexible RF photonic receivers and Software Defined Radios (SDRs). Although silicon photonics (SiP) is a promising technology platform to realize such receivers, process variations and lack of in-situ tuning capability limit the adoption of SiP filters in widely-tunable RF photonic receivers. To address this issue, this work presents a first 'in-situ' automatic reconfiguration algorithm and demonstrates a software configurable integrated optical filter that can be reconfigured on-the-fly based on user specifications. The presented reconfiguration scheme avoids the use of expensive and bulky equipment such as an Optical Vector Network Analyzer (OVNA), does not use simulation data for reconfiguration, reduces the total number of thermo-optic tuning elements required, and eliminates several time-consuming configuration steps as in the prior art. This makes this filter ideal in a real-world scenario where the user specifies the filter center frequency, bandwidth, required rejection, and filter type (Butterworth, Chebyshev, etc.), and the filter is automatically configured regardless of process, voltage, and temperature (PVT) variations. We fabricated our design in AIM Photonics' Active SiP process and have demonstrated our reconfiguration algorithm for a second-order filter with a 3dB bandwidth of 3 GHz, 2.2 dB insertion loss, and >30 dB out-of-band rejection using only two reference laser wavelength settings. Since the filter photonic integrated circuit (PIC) is fabricated using a CMOS-compatible SiP foundry, the design is manufacturable with repeatable and scalable performance suited for its integration with electronics to realize complex chip-scale RF photonic systems.**

***Index Terms*—Silicon photonics, optical filter, automatic tuning, integrated optics, thermal crosstalk, programmable photonics, reconfigurable optics, calibration, tuning algorithm, feedback control.**

I. Introduction

INTEGRATED radio-frequency (RF) photonics is rapidly emerging as a technology enabler of demanding application scenarios which require capabilities beyond those of traditional electronic systems. These capabilities include ultra-wide bandwidth, exceptional low latency, long-distance routing and immunity to electromagnetic interference (EMI) [1]–[6]. For any RF photonic integrated circuit (**IC**), optical filters are essential building blocks. The desirable feature that distinguishes RF photonic filters from their electronic, microwave, and micro-electromechanical systems (MEMS) counterparts is their tunability over a very wide range of center frequencies (1 to 100s of GHz) and very wide bandwidth. Consequently, RF photonic filters offer unprecedented reconfiguration capabilities (center frequency, bandwidth, filter type, and rejection) that are inconceivable with electronic ICs alone [2], [6]. These reconfiguration capabilities are highly desirable in many other applications in optical signal processing such as wavelength division multiplexing (WDM) [7], optical sensing and spectrometry [8], reconfigurable optical add/drop multiplexers [9], and quantum-correlated photon generation [10]. However, for their wider adoption in frequency-agile RF photonic receivers or Software Defined Radios (**SDR**), filter reconfiguration has to be rapid and in-situ, *i.e.*, automatic and free from any manual intervention [11].

Traditionally, RF photonic systems have been implemented using discrete and bulky photonic components that are power inefficient, expensive, and most importantly, are not amenable to the integration of complex systems. Silicon Photonics, on the other hand, leverages the unique capabilities of photonic signal processing while taking full advantage of the mature CMOS-like fabrication processes developed by the semiconductor industry [11]–[13]. This means, an optical filter realized in a silicon photonic platform is area and power efficient, robust, scalable, and can be manufactured on large-scale at a lower cost. However, due to process-induced random variations, any filter designed in a silicon photonic process will deviate from its intended characteristics. Therefore, a scheme is required that not only reconfigures the filter automatically but also is robust against the process, voltage, and temperature (**PVT**) variations.

Reconfiguration and tuning of integrated optical filters have been pursued in the literature. In ref. [14], only center frequency tuning was addressed whereas in refs. [15], [16], both center frequency and bandwidth were tunable. However, none of these works pursued out-of-band rejection tuning in the filter. Moreover, the filter reconfiguration was not fully automatic and heavily relied upon manual tuning. The first fully automatic tuning of silicon photonic filter was recently demonstrated in a path-breaking work by Choo et. al. in ref. [11]. However, the reconfiguration process involved the use of bulky and cost-prohibitive equipment, *i.e.*, an Optical Vector Network Analyzer (**OVNA**) to extract ring losses and FSR using Jones Matrix-based method [11], [17], [18]. As described in [17], [18], the process is extremely sensitive to the random polarization rotations on the Poincare sphere induced by the test setup. Therefore, it is not as straightforward as simply characterizing the filter with OVNA. The undesired artifacts introduced by the test setup's Jones matrix need to

The authors are with the Department of Electrical and Computer Engineering, University of Delaware, Newark, DE, 19716 USA e-mail: shawon@udel.edu.

This article has been accepted for publication in IEEE/OSA Journal of Lightwave Technology. This is the author's version which has not been fully edited and content may change prior to final publication. Citation information: DOI 10.1109/JLT.2022.3222131
Accepted Manuscript
Version of record at: https://doi.org/10.1109/JLT.2022.3222131

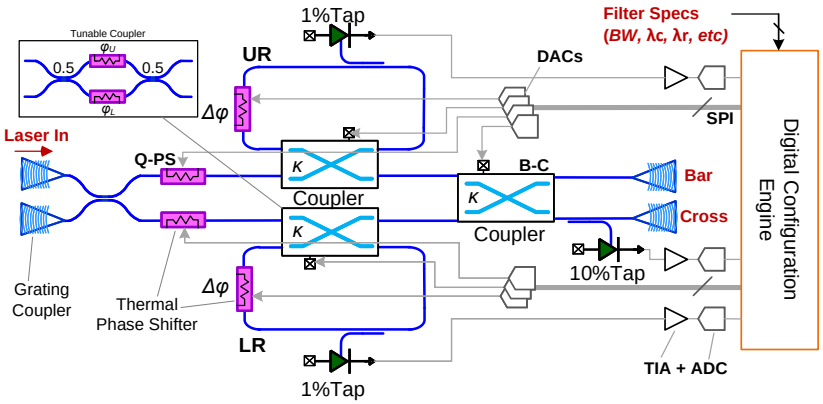

Fig. 1. Schematic of the silicon photonic filter and control electronics. The outer MZI is loaded with two rings coupled using a tunable coupler and includes microheater phase shifters. Another coupler is used to combine the two arms. Detector taps are placed at the drop port of the rings and on the filter cross port to assist the automatic reconfiguration algorithm. The inset shows the 2×2 switch used for realizing tunable couplers. Control electronics (DACs, TIAs, and ADCs) are interfaced with a digital configuration engine.

be resolved in a known reference frame. The extracted loss and FSR data are then fed to the simulation model to extract the coupling coefficient of the ring resonator. Therefore, due to the bulky nature of the OVNA as well as the complex extraction process, all calibration has to be done in-house, and consequently, no option for on-the-fly calibration.

The fundamental novelty of this work is that it achieves a truly in-situ automatic optical filter reconfiguration solution that has been experimentally demonstrated using a CMOS-compatible silicon-on-insulator (**SOI**) photonic process. We present an algorithm different from the one in ref. [11] which precludes the use of OVNA and eliminates several time-consuming steps during the reconfiguration process. In addition, our filter also uses less number of thermal tuning elements than [11]. The designed filter has a compact form factor and is the first such filter fabricated in AIM Photonics' Active Photonic process. Furthermore, a simplified analytical framework for the design of reconfigurable filters using analog switch-based couplers is provided and the filter PIC simulation leverages our open-source simulation code [19].

II. Filter Design, Fabrication, and Packaging

A. Filter Topology

The schematic of the second-order filter topology used in this work is shown in **Fig. 1**. The input continuous-wave (**CW**) laser is fed to both arms of an outer Mach Zehnder Interferometer (**MZI**) through a 3dB coupler. Each arm of the MZI is loaded with a microring (UR/LR) via a tunable coupler (UR-C/LR-C) and quadrature phase shifter (Q-PS). The two tunable couplers are in turn realized using a 2×2 MZI switch as shown in the inset of **Fig. 1**. Another tunable coupler (Back coupler, B-C) is used at the end of the MZI to allow control over the residual imbalance in the optical field between the two arms of the MZI caused by process variations. To monitor the ring resonance, a 1% tap followed by an on-chip Ge-photodetector (**PD**) is used in each ring. Although this directly translates to increased passband loss of the filter, these taps are an integral part of the automatic software reconfiguration algorithm [11]. Another 10% monitor tap is used at the cross port of the filter for out-of-band rejection tuning. The automatic calibration and tuning algorithms are implemented with the help of on-chip *thermo-optic phase shifters* or *microheaters*. Both arms of the outer MZI, both the rings and all three tunable couplers employ microheaters.

As mentioned earlier, the three tunable couplers used in the RF photonic filter are realized using 2×2 analog MZI switches. The coupling matrix, C, for these switches is expressed as [20]

$$C = je^{j\phi_A} \begin{bmatrix} \sin(\phi_D) & \cos(\phi_D) \\ \cos(\phi_D) & -\sin(\phi_D) \end{bmatrix} \tag{1}$$

$$\triangleq je^{j(\cos^{-1}(\sqrt{k})+\phi_{A_0})} \begin{bmatrix} \sqrt{t} & \sqrt{k} \\ \sqrt{k} & -\sqrt{t} \end{bmatrix} \tag{2}$$

Here, $\phi_A = \frac{\phi_U+\phi_L}{2} + \phi_{A_0}$ is the common-mode phase shift, $2\phi_D = \phi_U - \phi_L$ is the differential phase shift, and k and t are the cross and through optical power coupling coefficients respectively. The additional phase ϕ_{A_0} is the propagation delay in the switch due to its physical length. Moreover, ϕ_U and ϕ_L, are the phase shifts induced in the upper and lower arm microheaters in the switch respectively. By tuning ϕ_D, we obtain the power cross-coupling coefficient

$$k = cos^2(\phi_D) = \frac{1}{2}[1 + \cos(2\phi_D)] \tag{3}$$

$$\triangleq \frac{1}{2}[1 + \cos(\varphi_0 + \gamma P_c)] \tag{4}$$

and the through-coupling coefficient, $t = \sin^2(\phi_D)$. The (cross-)coupling coefficient k is tuned by applying microheater electrical power, P_c, to one of the two microheaters in the switch (i.e. $\phi_U = 2\phi_D$ and $\phi_L = 0$). This implies the common-mode phase shift is given by

$$\phi_A = \frac{\phi_U}{2} + \phi_{A_0} = \cos^{-1}(\sqrt{k}) + \phi_{A_0} \tag{5}$$

Also, in **Eq. 4**, φ_0 represents the random phase offset in the switch and γ is a proportionality constant relating the applied power to the thermo-optic phase shifter.

The z-domain through (all-pass) and drop (bandpass) transfer functions of a single ring in the filter seen in **Fig. 1** are derived as-

$$A_{thru}(z) = e^{j\phi_A} \cdot \frac{j\sqrt{t} - \sqrt{t_m} a e^{j(\phi+\phi_A)} z^{-1}}{1 + j\sqrt{t t_m} a e^{j(\phi+\phi_A)} z^{-1}} \tag{6}$$

$$A_{drop}(z) = \frac{\sqrt{k k_m} e^{j\phi_A} z^{-1/2}}{1 + j\sqrt{t t_m} a e^{j(\phi+\phi_A)} z^{-1}} \tag{7}$$

where $k_m = 0.01$ and $t_m = 0.99$ are the cross- and through-coupling coefficients for the 1% monitor, and $a = e^{-\alpha L} < 1$ is the loss factor in the ring and L is the ring length. Here, α is the field attenuation coefficient and our single-mode SOI waveguide loss is 2-2.5dB/cm [21].

A desired filter polynomial, G(z), can be synthesized using the coupled all-pass decomposition (**APD**) method by employing the sum and difference of two all-pass filters (**APF**), A_1 and A_2, as $G(z) = \frac{1}{2}(A_1(z) + A_2(z))$ and $H(z) = \frac{1}{2}(A_1(z) - A_2(z))$. For even-order filters, we have $A_2(z) = A_1^*(z^*)$ [23], [24]. The 2^{nd}-order APD filter seen in **Fig. 1** had two ring APF arms and the sum or difference is realized using the back-coupler, B-C. The resulting filter output bar and cross transfer functions are

$$G(z), H(z) = \frac{j}{\sqrt{2}} \Big(\sqrt{k_{bc}} e^{j\phi_{q,ps}} A_{thru}(z)\Big|_{k_1,\phi_1} \pm \sqrt{t_{bc}} e^{-j\phi_{q,ps}} A_{thru}(z)\Big|_{k_2,\phi_2} \Big) \tag{8}$$

In our notation, k_n and ϕ_n are the power coupling coefficient and phase shift in the n^{th} ring, k_{bc} and $t_{bc} = 1 - k_{bc}$ are the back-coupler cross and through coupling coefficients, and $\phi_{q,ps}$ is the quadrature phase shift.

B. Filter Synthesis

Filter design starts with the synthesis of a polynomial, G(z), for the specified filter type and specifications. Then the denominators of the coupled all-pass polynomials, $D_{1,2}(z)$, corresponding to G(z), and constant phase β were obtained using the ***tf2ca*** function in Matlab™. Then numerators were obtained using $N_1(z) = \textbf{\textit{fliplr}}(D_1^*(z))$ and $N_2(z) = \textbf{\textit{fliplr}}(D_2^*(z))$. This yielded the two all-pass transfer functions $A_1(z) = e^{j\beta}\frac{N_1(z)}{D_1(z)}$ and $A_2(z) = A_1^*(z^*) = e^{-j\beta}\frac{N_2(z)}{D_2(z)}$. Next, the all-pass transfer functions $A_{1,2}(z)$ are mapped to the (cascade of) ring resonators in the upper and lower arms. If the roots of denominators $D_1(z)$, i.e. the poles of $A_1(z)$, are p_n, then the cross-coupling coefficients are determined using $k_n = (1 - |p_n|^2)$ and $t_n = |p_n|^2$. The phase $\phi_n = \angle p_n$. The quadrature phase shift for the upper arm is obtained as $\phi_{q,ps} = \beta - \sum_n \phi_n$. The lower arm coupling coefficients are identical to those of the upper arm, and ϕ_n and $\phi_{q,ps}$ are of opposite sign, representing the conjugate APF responses. The synthesized Butterworth filter coefficients for the filter specifications are listed in Table I.

TABLE I
FILTER COEFFICIENTS FOR THE SECOND-ORDER APD-TYPE OPTICAL FILTER.

Ring (n)	k_n	ϕ_n	$\phi_{q,ps}$
1 (UR)	0.4385	-0.2969	Top: -1.6137
2 (LR)	0.4385	0.2969	Bot: 1.6137

C. PIC Design and Fabrication

The filter was designed and fabricated in AIM Photonics foundry's 300mm Active Photonics process [22], [25]. **Fig. 2** shows a 3D visualization of the filter schematic seen in **Fig. 1**, and the process cross-section. This process features silicon-on-insulator (SOI) rib and ridge waveguides, silicon nitride waveguides, escalators, modulator doping, Germanium (Ge) detectors, and three metal layers for routing [25]. The PIC layout employed several process-optimized components from the PDK library [21]. Grating couplers (**GC**) were used for vertical coupling of light into the PIC. Single-mode silicon waveguides of 480nm width and 220nm height were used for routing and interconnecting the optical components in TE polarization. The analog 2×2 switches were realized using doped silicon waveguide microheater sections and 3-dB couplers [26], and with a measured thermo-optic time-constant of $\sim 15\mu$s. The physical lengths of the microheaters and 2×2 switches are around $100\mu m$ and $550\mu m$, respectively.

The filter was simulated using Lumerical Interconnect [27] with the AIM PDK library, as well as our open-source Python-based PIC simulator [19] built using the PhotonTorch photonic simulation framework [28]. **Fig. 3**(a) shows the simulated bar and cross responses of the filter after including all PIC parameters including the losses and delays. The peaks of the optical monitors are aligned to the desired resonance frequency (or wavelength), corresponding to the ring phase, ϕ_n, for each of the rings. The simulated passband loss using the synthesized filter coefficients was ∼2.2 dB due to the ring losses with a 3dB bandwidth (BW) of 3 GHz and an out-of-band rejection of >30dB. The pole-zero plots for APFs, and bar and cross responses, i.e. $G(z)$ and $H(z)$ respectively, are shown in **Fig. 3**(b).

The filter layout was compacted as much as possible to share the photonic chip with other RF photonic circuits. The rings were routed in a compact serpentine fashion with a 30μm bend radius for lower loss and reflections. The resulting total physical length of the rings was $\sim 2200\mu m$ each, with a corresponding free-spectral range (**FSR**) of around 31GHz. The monitor taps were realized using 1% and 10% couplers, Ge waveguide detectors, and waveguide terminations. The filter die micrograph is shown in **Fig. 4(a)**. The filter core layout occupied 1.12 mm^2 area on this chip.

D. Packaging and Electronic Back-end

The fabricated PIC die was polished down to $150\mu m$ and packaged in a chip-on-board (**COB**) assembly as shown in **Fig. 4(b & c)**. A Peltier cell and thermistor were used along with a thermo-electric cooler (**TEC**) controller in a closed-loop to stabilize the temperature of the chip and to minimize the thermal crosstalk among the on-chip tuning elements. The

This article has been accepted for publication in IEEE/OSA Journal of Lightwave Technology. This is the author's version which has not been fully edited and content may change prior to final publication. Citation information: DOI 10.1109/JLT.2022.3222131
Accepted Manuscript
Version of record at: https://doi.org/10.1109/JLT.2022.3222131

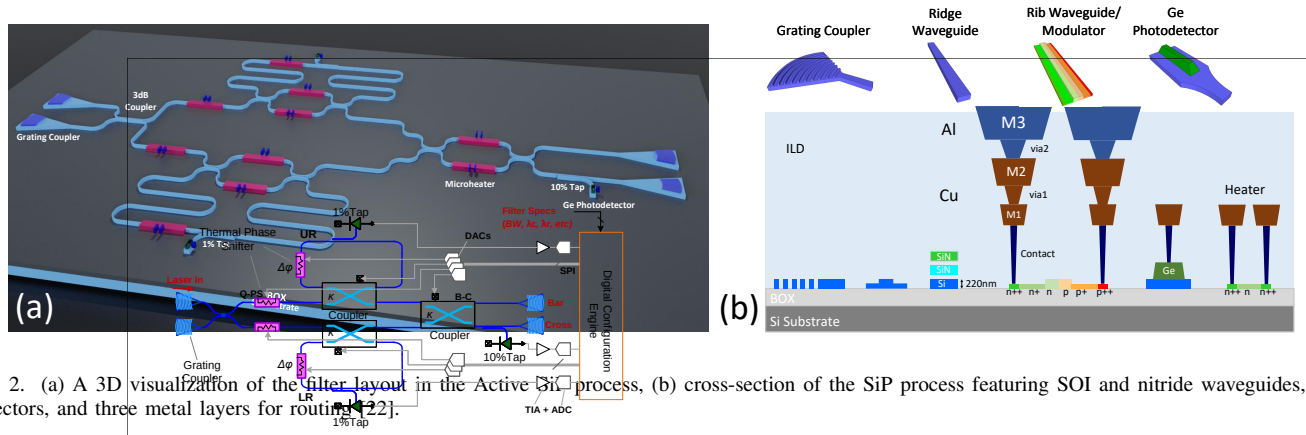

Fig. 2. (a) A 3D visualization of the filter layout in the Active Si process, (b) cross-section of the SiP process featuring SOI and nitride waveguides, Ge detectors, and three metal layers for routing [22].

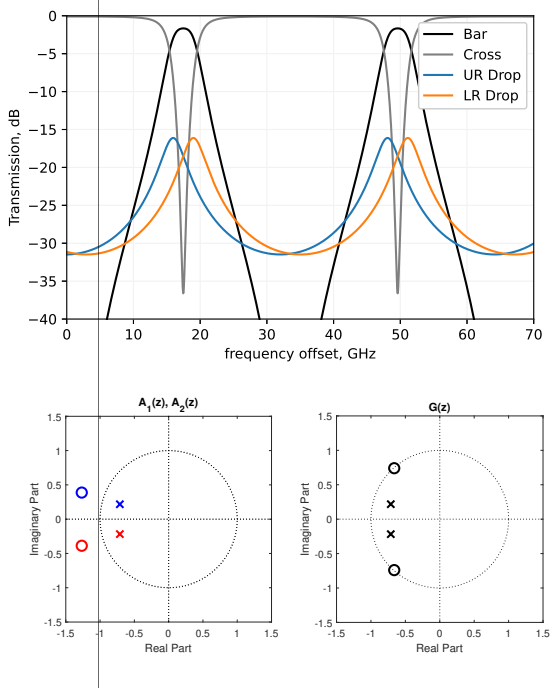

Fig. 3. (a) Transmission response of the second-order APD-type filter simulated using custom PhotonTorch-based code and the SiP process data. (b) Complex z-plane pole-zero plots for $G(z)$ and $A_{1,2}(z)$.

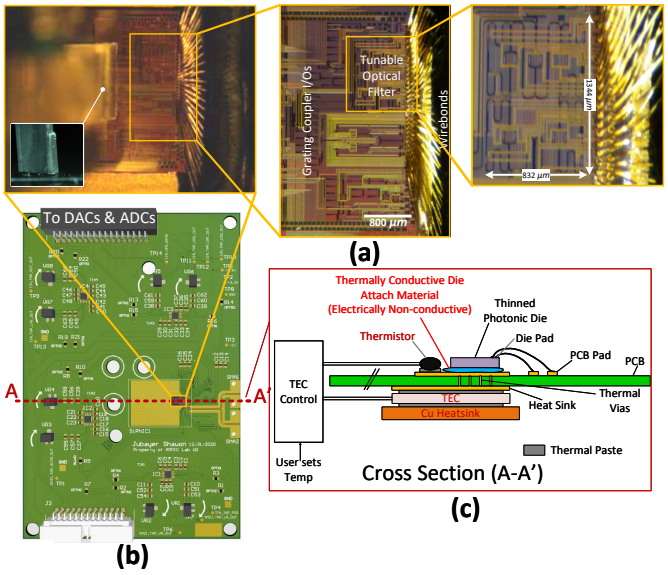

Fig. 4. (a) Chip micrograph of the silicon photonic filter fabricated in the AIM Photonics process. (b) The chip is attached and wire-bonded onto a custom-designed printed circuit board (PCB) using Chip-On-Board (COB) packaging. The PCB contains transimpedance amplifiers (TIAs) and ribbon cable interfaces to another electronic board with DACs and ADCs. (c) The COB assembly is co-packaged with a thermistor on the top side and a Peltier cell on the back side of the PCB with an external TEC controller board in a closed loop.

combination of die thinning and TEC at the bottom of the die provides effective thermal isolation by creating a prominent thermal gradient in the vertical direction [11].

The electrical pads were placed on two rows on the East edge of the PIC which were wire-bonded with two rows of PCB pads. The optical monitors were connected to the on-board transimpedance amplifiers (**TIAs**), whose outputs were interfaced with commercial off-the-shelf (COTS) 16-bit analog-to-digital converters (**ADCs**) using a ribbon cable. These pads provide 16-bit digital-to-analog converters (**DACs**) interfaces to the microheaters. All the DACs and ADCs communicate via SPI interface with a microcontroller, which provides a software abstraction to the algorithm code.

The operating voltage range of the microheaters is from 0 to 5V and requires a power of $P_\pi < 30$mW for an optical phase shift of π. These voltage ranges are CMOS-compatible and the microheater driver circuits can be implemented using stacked high-voltage I/O transistors with a 5V supply voltage in 65nm CMOS (or similar) process technology [29], [30]. The TIA interface with the PDs and the 16-bit DACs and ADCs can be designed using the standard transistors in CMOS, allowing future integration of all electronics on the same chip.

E. Portability

It is important to note that we used a precise alignment grating coupling stage in this work. However, this is merely part of our optical setup and will conveniently be replaced by attached fiber arrays in a portable solution [31], [32]. We also used an external laser only for demonstration purposes. In the actual portable solution, this external laser will either be

This article has been accepted for publication in IEEE/OSA Journal of Lightwave Technology. This is the author's version which has not been fully edited and content may change prior to final publication. Citation information: DOI 10.1109/JLT.2022.3222131
Accepted Manuscript
Version of record at: https://doi.org/10.1109/JLT.2022.3222131

replaced by a heterogeneously integrated semiconductor laser [33] or a discrete tunable laser in a butterfly package [34]. Since our tuning algorithm is independent of the implementation of the laser, the algorithm can reconfigure the filter at the desired center frequency and BW as long as the filter receives an optical stimulus.

Also, as mentioned before, prior art used OVNA to extract the loss and FSR of the individual ring resonators in the optical filter. The OVNA is a bulky and expensive instrument. On the other hand, our in-situ extraction method is not only simpler and fully-automated but also can be implemented in a portable form factor, and the filter parameters can be extracted on the fly, as and when needed. The SMU we need for our parameter extraction is available in a compact chip-scale form factor [35]. Fig. 5a shows the schematics of our test setup whereas Fig. 5b illustrates the schematics of the application test setup when SMU is implemented on chip. The snapshot of the experimental setup used in this work for the demonstration of the filter is shown in Fig. 5c & d.

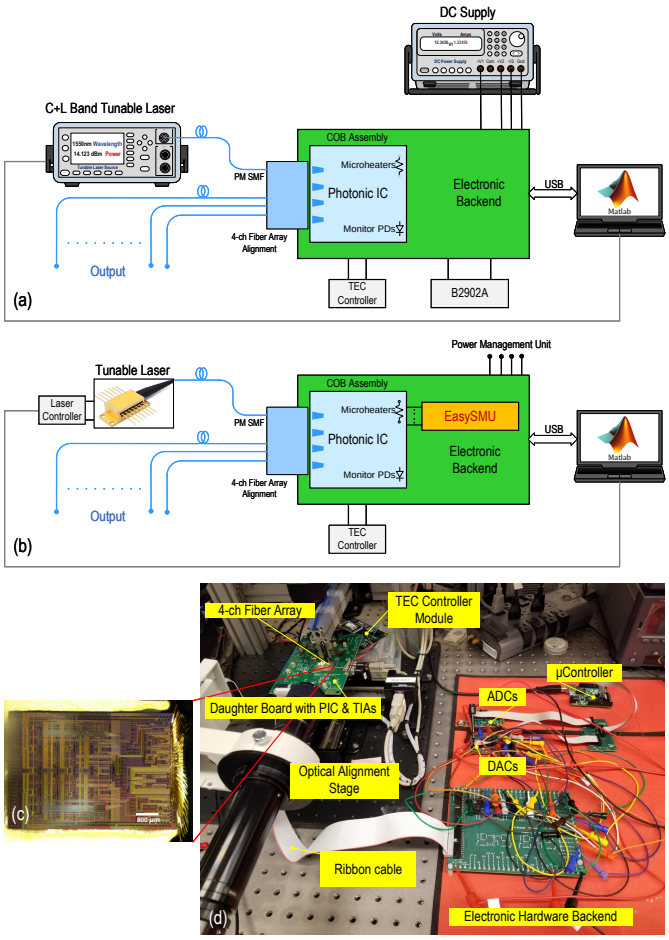

Fig. 5. (a) Schematics of the test setup used in this work for the demonstration of the filter. (b) Schematics of the application test setup when SMU is implemented on chip. The tunable laser is implemented in a small form factor (butterfly package). (c) The silicon photonic chip wirebonded onto a PCB. (d) The experimental setup used for the demonstration of the filter. Here, the silicon photonic die is co-packaged with on-board TIAs and the DACs & ADCs (implemented on separate boards) are controlled by a microcontroller via SPI interface.

F. Other Filter Tuning Mechanisms

Several other optical filter tuning mechanisms have been explored in the literature. These include electro-optic, acousto-optic, MEMS-based, and piezoelectric. Since the thermo-optic effect is the strongest in SOI waveguides and heaters realized using doped-waveguides or metals don't require complex fabrication steps or foundry-incompatible materials, microheaters are the most commonly-used method for tuning foundry-fabricated PICs [36]. Alternative tuning schemes may mitigate the thermal crosstalk, but they have their own limitations which are described as follows:

1) Electro-optic effect: Electro-optic effect in silicon is obtained by forming a depletion-mode or injection-mode *pn*-junction in the silicon waveguide and uses plasma dispersion effect for inducing voltage-dependent phase shift [36], [37]. However, due to the weak electro-optic effect, a typical 2π phase shift would require nearly cm-long phase shifters [38], as opposed to the $100\mu m$ compact thermo-optic phase shifters used in this work. These long phase shifters will limit the FSR to below 10GHz. Furthermore, optical absorption in the doped-regions would incur significant insertion loss, making the scheme impractical.

2) Acousto-optic effect: Acousto-optic effect utilizes *stimulated Brillouin scattering* (**SBS**), whereby phonons, or acoustic waves, perturb the waveguide permittivity and shape through photoelasticity. This perturbation causes an optical pump mode to be shifted by the phonon frequency [39]. While SBS has been demonstrated in chalcogenides with large optical nonlinearity, such as As_2S_3 waveguides [40], SOI waveguides do not produce efficient Brillouin nonlinear interactions due a small photoelastic tensor component (p_{12}) and leakage of acoustic waves into the substrate. Specialized waveguide structures such as suspended waveguides have been used to exhibit SBS in silicon [39], however, these require customized fabrication which is typically not available in SiP foundry processes. In addition, an optical pump and long Brillouin-active waveguide structures are required for realizing a large SBS gain for each of the components to be tuned [39], [41]. These will inevitably complicate the PIC design and may not scale to complex filters such as the one used in this work.

3) MEMS tuning: Micro-optoelectromechanical systems (**MOEMS**), also known as optical MEMS, could theoretically replace the thermo-optic phase shifters and couplers in the filter [42]. However, these structures require specialized fabrication of suspended waveguide structures with controlled dielectric and substrate etching steps, require complex hermetic packaging, and incur low fabrication yield [43]. Also, these require large drive voltages for electrostatic actuation. The scaling of PICs with optical MEMS components will be fundamentally limited by the lower yield and reliability of the moving parts.

4) Piezoelectric effect: Piezoelectric tuned devices are similar to optical MEMS, whereby a suspended waveguide is processed with a thin-film piezoelectric actuator, such as the one fabricated with Lead Zirconate Titanate (PZT). The voltages needed for actuating these devices are lower than the electrostatically-tuned optical MEMS devices [44]. However,

This article has been accepted for publication in IEEE/OSA Journal of Lightwave Technology. This is the author's version which has not been fully edited and content may change prior to final publication. Citation information: DOI 10.1109/JLT.2022.3222131
Accepted Manuscript
Version of record at: https://doi.org/10.1109/JLT.2022.3222131

these also require additional processing and materials in the foundry process [45].

III. In-Situ Component Parameter Extraction

To reconfigure the SiP filter, device parameters such as the coupling ratio of the tunable couplers (k_n) and the ring phase bias (ϕ_n) for the selected center wavelength (λ_c) need to be configured. Here, $n = 1, 2, \ldots N$ stands for the ring number. These parameters are controlled by the DAC voltage (or power). Due to PVT variations in the photonic chip, there is a significant variation in the response of the tunable couplers and the phase shifters with respect to the applied power. Thus, no two couplers (or phase shifters) produce the same coupling (phase shift) for a given applied DAC voltage.

The phase shift, ϕ_n, produced by the microheaters linearly depends upon the applied electrical power, P_n, as

$$\phi_n = \gamma P_n = \frac{\pi P_n}{P_\pi} \tag{9}$$

However, the microheater resistance, R, exhibits nonlinearity due to self-heating. Thus, applied electrical power has a nontrivial nonlinear dependence on the applied DAC voltage, $P_n = f(v_n) \neq \frac{v_n^2}{R}$. This P_n *vs* v_n characteristics must also be extracted so that we can accurately configure component parameters on the chip using the DACs. This necessitates a one-time in-situ pre-characterization of each of these components, and subsequently the configuration of them, as they are used. In this section, we provide algorithms for these pre-characterization routines and configurations.

Each of these component characterizations has two steps- Part I and II. The first part, Part I, for either k_n or ϕ_n extraction represents the component pre-characterization phase. On the other hand, during the automatic reconfiguration phase, this pre-characterized data is used for in-situ estimation and configuration of k_n and ϕ_n parameters in the on-chip filter. Part II algorithms for both k_n and ϕ_n represent these in-situ estimations and configurations.

It is important to note that Part I is a one-time operation and does not need to be repeated again as long as the filter ambient temperature is kept the same as the filter pre-characterization temperature. This is ensured by using the TEC setup seen in **Fig. 4**. On the other hand, Part II algorithms are invoked each time the filter is reconfigured or tuned to a different center frequency (or wavelength).

A. Coupling Ratio (k_n) Extraction

During the initial pre-characterization routine, **Algorithm 1** is executed for each of the n rings in the filter. Here, to be able to configure the desired coupling ratio (k_n) of the tunable coupler of the nth ring, the wavelength response of the ring drop-port is recorded (using the monitor PDs) for a range of coupler input voltages ($v_{n,c}$). From this data, the voltage ($v_{n,cm}$) corresponding to the **maximum coupling ratio** ($k_{n,max}$) is recorded. The maximum coupling is identified by observing the quality factor (Q) of the ring drop-port resonance. Optical cavity dynamics dictate that as the coupling ratio approaches unity, ring Q decreases [46]. This provides the basis for identifying the $k_{n,max}$ by observing the **minimum Q** (as shown in the bottom-right inset of **Fig. 6**). On the other hand, zero-coupling voltage ($v_{n,c0}$) is identified simply by finding the $v_{n,c}$ corresponding to the lowest monitor output at a fixed $\lambda \in \Lambda$ (any wavelength within one FSR in the wavelength range of interest, *i.e.* Λ). This is possible due the to very low optical power coming through the drop-port when zero-coupling is in place (as shown in the top-left inset of **Fig. 6**). Afterwards, the power ($P_{n,c}$) delivered to nth coupler microheater at different $v_{n,c}$ is recorded using a Keysight B2902A source measurement unit (**SMU**), and thus the $P_{n,c}$ *vs* $v_{n,c}$ characteristics are obtained. The SMU can also be realized using on-board electronics for portability [35].

Utilizing this data rather than simply relying on the quadratic relationship between voltage and power [47] ensures that the algorithm is insensitive to the electrical non-linearity of on-chip microheaters. Subsequently, the zero-coupling power ($P_{n,c0}$) and max-coupling heater power ($P_{n,cm}$) are obtained, and thus the power (P_{n,c_π}) required to obtain a π phase shift in the coupler microheaters is determined as $P_{n,c_\pi} = P_{n,cm} - P_{n,c0}$. This P_{n,c_π} will subsequently serve as a reference value for the tuning algorithm to operate at different wavelengths within the FSR of the rings. It is important to note that by utilizing zero and maximum coupling rather than the critical coupling as in [11], we avoid repeated re-centering of the ring resonance at the filter center frequency (λ_c) during the k_n extraction step. Also as mentioned earlier, the use of an OVNA is avoided by precluding the ring loss measurements at critical coupling for each of the rings as in the prior art in [11]. This considerably speeds up the k_n extraction step in the filter reconfiguration algorithm (>2X reduction in time) and enables in-situ tuning that can be implemented using PCB-level or chip-scale electronics.

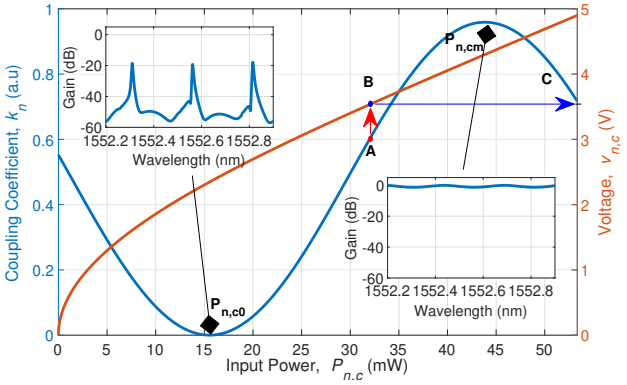

Fig. 6. (Illustration of Algorithms 1 and 2): Coupling coefficient, k_n, of a tunable coupler with a process induced random phase offset and the microheater voltage as a function of input power, $P_{n,c}$, as expressed by **Eq. 4**. The top-left and bottom-right insets show the normalized wavelength response of the ring drop port with its coupler set at zero ($P_{n,c} = P_{n,c0}$ & $k = 0$) and maximum coupling ratio ($P_{n,c} = P_{n,cm}$ & $k = k_{n,max}$), respectively. Any desired value for $k = k_n$ (labeled as **A**) can be in-situ configured by applying the corresponding input power, $P^*_{n,c}$ (label **B**), which in turn is translated to the DAC voltage, $v^*_{n,c}$ (label **C**).

During the in-situ reconfiguration routine in **Algorithm 2**, first, the $P_{n,c0}$ is recorded and depending on the λ_c, this may not be the same as the $P_{n,c0}$ seen in **Algorithm 1**. Then,

This article has been accepted for publication in IEEE/OSA Journal of Lightwave Technology. This is the author's version which has not been fully edited and content may change prior to final publication. Citation information: DOI 10.1109/JLT.2022.3222131
Accepted Manuscript
Version of record at: https://doi.org/10.1109/JLT.2022.3222131

Algorithm 1 Coupling ratio extraction (Part I)

Start
Get nth Ring drop-port response, $f(\lambda, v_{n,c})$ & estimate Q
$v_{n,cm}$, $P_{n,cm} \leftarrow$ **Find** $v_{n,c}$, $P_{n,c}$ corresponding to **min**(Q)
Set laser wavelength at $\lambda \in \Lambda$
Get nth Ring drop-port response, $f(v_{n,c})$
$v_{n,c0}$, $P_{n,c0} \leftarrow$ **Find** $v_{n,c}$, $P_{n,c}$ for zero coupling from **min**$(f(v_{n,c}))$
$P_{n,c_\pi} \leftarrow P_{n,cm} - P_{n,c0}$
Save P_{n,c_π}
Save $v_{n,c}$ *vs* $P_{n,c}$ characteristics
End

the raised-cosine coupling ratio *vs* power curve of the tunable coupler [11] from **Eq. 4** and illustrated in **Fig. 6** is fitted to the ($P_{n,c0}$, 0) & ($P_{n,c0}+P_{n,c_\pi}$, $k_{n,max}$) data points. From this fitted curve, power ($P^*_{n,c}$) required to set any desired coupling ratio (k_n) is estimated as shown in **Fig. 6**. Afterwards, from the pre-characterization $v_{n,c}$ *vs* $P_{n,c}$ data, the DAC voltage ($v^*_{n,c}$) needed to set a desired k_n is determined. Here, $k_{n,max}$ is the maximum coupling coefficient and due to the intrinsic loss in the coupler, it never reaches unity. For our tunable coupler, it is found to be 0.959 from the foundry PDK. Furthermore, for the purpose of the filter and its usable frequency range for a free-spectral range (FSR) of 31 GHz (or 0.249 nm), the couplers can be considered broadband. Thus, all the extracted parameters are usable at any frequency (or wavelength) within the FSR.

Algorithm 2 Coupling ratio extraction (Part II)

Input: $k_n \leftarrow$ User specifies the desired coupling coefficient
procedure ccoeff(n, λ_c, k_n)
    Set laser wavelength at λ_c
    Get nth Ring drop-port response, $f(v_{n,c})$
    $v_{n,c0}$, $P_{n,c0} \leftarrow$ **Find** $v_{n,c}$, $P_{n,c}$ for zero coupling from **min**$(f(v_{n,c}))$
    Fit k_n *vs* $P_{n,c}$ in **Eq. 4** using ($P_{n,c0}$, 0) & ($P_{n,c0}+P_{n,c_\pi}$, $k_{n,max}$) data points
    $P^*_{n,c} \leftarrow$ **Find** power for k_n from the above curve-fit
    $v^*_{n,c} \leftarrow$ **Find** voltage corresponding to $P^*_{n,c}$ from $v_{n,c}$ *vs* $P_{n,c}$ data
    Return nth coupler DC bias, $v^*_{n,c}$
End procedure

B. Ring Phase (ϕ_n) Extraction

Now we describe the one-time pre-characterization routine (i.e. **Algorithm 3**) for the ring phase bias. First, all the rings except for the nth ring are detached from the filter by setting their corresponding couplers to zero-coupling. This ensures that the cross-port of the filter only contains the resonance information of the nth ring. Then, the voltage (v_{n,r_π}) required for a π phase shift in the ring microheater was extracted by monitoring the cross port of the filter and shifting the resonance by full FSR (corresponding to 2π phase-shift in the ring) for the applied voltage. Afterwards, the power ($P_{n,r}$) delivered to nth ring heater at different $v_{n,r}$ is recorded using the SMU and P_{n,r_π} is obtained. As mentioned before, utilizing $v_{n,r}$ *vs* $P_{n,r}$ data ensures that the algorithm is insensitive to the process-dependent electrical nonlinearity of the on-chip microheaters.

During the automatic calibration routine in **Algorithm 4**, pre-characterized P_{n,r_π}, and $v_{n,r}$ *vs* $P_{n,r}$ characteristics of the ring microheater is utilized. Then, from the phase-shift desired

Algorithm 3 Ring phase extraction (Part I)

Start
Set $v_{i,c} \leftarrow$ **Find** $v_{i,c0}$ for all couplers except when $i = n$
Get filter cross-port response, $f(\lambda, v_{n,r})$
v_{n,r_π}, $P_{n,r_\pi} \leftarrow$ **Find** $v_{n,r}$, $P_{n,r}$ for π phase-shift, obtained using a full-FSR sweep
Save P_{n,r_π}
Save $v_{n,r}$ *vs* $P_{n,r}$ data
End

by the user, ϕ_n, the required microheater power change, $\Delta P_{n,r}$, is estimated using **Eq. 9** as

$$\Delta P_{n,r} = \frac{\phi_n P_{n,r_\pi}}{\pi} \tag{10}$$

Meanwhile, the voltage ($v_{n,res}$) for which the nth ring resonance is aligned with λ_c is obtained by sweeping the ring microheater voltage ($v_{n,r}$) and finding the maximum drop port response. From this data, the power ($P_{n,res}$) at which ring resonance is aligned with λ_c is obtained. Then, the power ($P^*_{n,r}$) required to set the ring at desired ϕ_n is estimated as $P^*_{n,r} = P_{n,res}+\Delta P_{n,r}$ and the corresponding ring microheater voltage ($v^*_{n,r}$) is applied.

Algorithm 4 Ring phase extraction (Part II)

Input: $\phi_n \leftarrow$ User specifies the desired ring phase
procedure ringbias(n, λ_c, ϕ_n)
    $\Delta P_{n,r} \leftarrow \frac{\phi_n P_{n,r_\pi}}{\pi}$
    Set laser wavelength at λ_c
    Get nth Ring drop-port response, $f(v_{n,r})$
    $v_{n,res}$, $P_{n,res} \leftarrow$ **Find** $v_{n,r}$, $P_{n,r}$ for **max**$(f(v_{n,r}))$ ▷ resonance
    $P^*_{n,r} \leftarrow P_{n,res} + \Delta P_{n,r}$
    $v^*_{n,r} \leftarrow$ **Find** voltage for $P^*_{n,r}$ from the $v_{n,r}$ *vs* $P_{n,r}$ data
    Return nth ring heater DC bias $v_{n,res}$ & $v^*_{n,r}$
End procedure

IV. Automatic Tuning of Filters

The filter tuning algorithm (**Algorithm 5**) starts off with the user specifying the desired filter specifications. The APD filter synthesis algorithm [24], [48], [49] translates these user-defined specifications (filter type, order, bandwidth, center frequency, out-of-band suppression) to filter parameters (k_n, ϕ_n & $\phi_{q,ps}$) for all rings and MZI arms. Then the **ccoeff**(n, λ_c, k_n) routine from **Algorithm 2** is invoked and desired coupling coefficients for all ring couplers are configured by setting the microheater voltages of the ring tunable couplers to $v^*_{n,c}$. Next, the **ringbias**(n, λ_c, ϕ_n) routine from **Algorithm 4** is invoked to set all the ring biases (ϕ_n) with respect to the λ_c at their desired values. It's important to note that due to thermal crosstalk between on-chip microheaters, every time a ring phase (ϕ_n) is set, previously aligned rings get de-tuned and several iterations are required accurately to set all the ϕ_n values.

To improve the out-of-band rejection of the filter, we maximize the 10% monitor tap placed at the cross-port of the filter at λ_r by tuning the MZI quadrature phase shifter (Q-PS) and the back-coupler (B-C) [11]. Here, λ_r is the wavelength where a null in the filter response can be enforced.

However, the out-of-band-rejection calibration via Q-PS and B-C microheaters shifts the resonance of the previously tuned

This article has been accepted for publication in IEEE/OSA Journal of Lightwave Technology. This is the author's version which has not been fully edited and content may change prior to final publication. Citation information: DOI 10.1109/JLT.2022.3222131
Accepted Manuscript
Version of record at: https://doi.org/10.1109/JLT.2022.3222131

rings, thus altering the center wavelength (or frequency) of the filter response. To perform center-wavelength correction, rings, Q-PS and B-C are tuned subsequently and several iterations of tuning (n rings, Q-PS, and B-C) are needed to reach the thermal steady-state of the PIC. When the required voltage stimulus is stabilized within a tolerance range (indicating a thermal steady-state), the filter tuning is complete.

It's important to note that the coupling ratios of the tunable couplers are relatively stable in presence of thermal perturbation. This is due to the fact that thermal perturbations coming from other microheaters affect both microheaters of the tunable couplers almost equally, thus inducing a 'common-mode' phase shift that does not alter the coupling ratios which only depends upon the differential phase (ϕ_D). Therefore, it is not required to include ring coupler tuning inside the iteration loop, which in turn speeds up the reconfiguration process. Another key aspect of this algorithm is that it precludes the use of 'outer ring' for out-of-band rejection in [11], thus further reducing configuration time for 'outer ring' resonance alignment and also resulting in a smaller layout area.

Algorithm 5 Nth Order Filter reconfiguration Algorithm

Start
Get Filter specifications (Type, Order, BW, Rejection, λ_c, λ_r) from the user
k_n, ϕ_n, $\phi_{q,ps}$ $\leftarrow$ APD filter synthesis using the specifications
Set $n = 1$
while $n \leq N$ **do**
    Invoke [$v^*_{n,c}$] = ccoeff(n, λ_c, k_n) routine
    Set $v^*_{n,c} \leftarrow$ DC bias of nth coupler
    Set $n = n + 1$
end while
Set $n = 1$
while err$_j \geq$ tol$_j$ **do**
    while err$_i \geq$ tol$_i$ **do**
        while $n \leq N$ **do**
            Invoke [$v_{n,res}$, $v^*_{n,r}$] = ringbias(n, λ_c, ϕ_n)
            Set $v_{n,res} \leftarrow$ DC bias for nth ring resonance
            Set $n = n + 1$
        end while
        Calculate err$_i$
    end while
    Set $v^*_{n,r} \leftarrow$ DC bias of nth ring
    Set Laser wavelength at λ_r
    Get filter cross-port PD response, $f(v_{q,ps})$
    $v_{q,psm} \leftarrow$ **Find** $v_{q,ps}$ for **max**$f(v_{q,ps})$
    Set DC bias of the arm phase shifter at $v_{q,psm}$
    Get filter cross-port PD response, $f(v_{b,c})$
    $v_{b,cm} \leftarrow$ **Find** $v_{b,c}$ for **max**$f(v_{b,c})$
    Set DC bias of back-end tunable coupler at $v_{b,cm}$
    Calculate err$_j$
end while
End

V. Experimental Results

To demonstrate the functionality and efficacy of the proposed reconfiguration algorithm, the 2nd-order Butterworth filter was experimentally reconfigured using the coefficients from **Table I**. This filter is intended for ∼30dB out-of-band rejection, an insertion loss (IL) of 2.2 dB, and the 3dB bandwidth (BW) of 3 GHz at 1550nm wavelength. The 1550nm CW laser and input/outputs were coupled into the PIC using a 4-channel polarization maintaining fiber array. The fiber array was automatically aligned to the on-chip GCs.

The experimentally measured response of the filter at different stages of reconfiguration is illustrated in **Fig. 7**. The observed GC response exhibited ∼0.8dB ripple in the passband response, and the passband GC losses were de-embedded from the filter response. Unlike [11], here in this work, as soon as the Q-PS and/or B-C microheater is tuned, the previously locked UR & LR rings get de-tuned due to thermal crosstalk and the center frequency of the filter shifts from its intended λ_c (in this case, λ_c = 1550 nm) as demonstrated in **Fig. 7**(d) and (e). Therefore, several iterations are required for the automatic tuning of the filter.

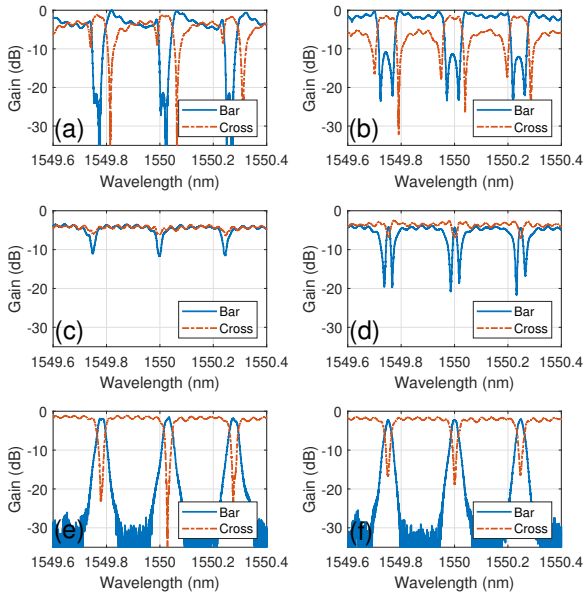

Fig. 7. Experimentally measured bar and cross port responses (normalized) of the filter: (a) When powered up without any tuning, (b) After all the coupling ratios (k_n) of the rings are configured (Algorithm 2), (c) After aligning the ring resonances to λ_c (part of Algorithm 4), (d) After setting desired phase bias (ϕ_n) of the rings (part of Algorithm 4), (e) After Quadrature Phase Shifter (Q-PS) and Back-Coupler (B-C) tuning, (f) After center frequency correction i.e. several iterations of ring phase bias (ϕ_n), Q-PS and B-C tuning.

Since DACs set the microheater voltages (or power), the convergence of the tuning algorithm can be observed in the settling of the DAC output voltages. In **Fig. 8**, the transient evolution of DAC voltages for all relevant microheaters during the tuning process is presented. **Fig. 8** also shows the laser wavelength settings (λ_c and λ_r) that are applied to the filter input. Key events that occur during the automatic tuning process are labeled in **Fig. 8** and explained in **Table II**. This figure shows three iterations to tune the filter (rings, Q-PS & B-C), and the time taken for the iteration progressively decreases as the filter gets closer to the thermal steady-state during tuning. In our filter layout, the Q-PS and B-C coupler were in close proximity to the rings resulting in substantial thermal crosstalk. The fabricated filter takes around 725 seconds to reconfigure. The long configuration times are primarily determined by the thermal crosstalk between the components and can be significantly reduced by spreading out

This article has been accepted for publication in IEEE/OSA Journal of Lightwave Technology. This is the author's version which has not been fully edited and content may change prior to final publication. Citation information: DOI 10.1109/JLT.2022.3222131
Accepted Manuscript
Version of record at: https://doi.org/10.1109/JLT.2022.3222131

the layout and by employing microheaters with undercut for thermal isolation [50], [51].

As mentioned earlier, for software defined radios (SDR) and flexible RF photonic receivers, it is vital to have filters with agile center-frequency and bandwidth tunability. To demonstrate such capability, we reconfigured the filter at 5 different center frequencies (λ_c) with 0.05nm (∼6.25 GHz) spacing as shown in **Fig. 9** (top). It's important to note that the center frequency tuning is continuous and any center wavelength (λ_c) can be configured as long as it is within the FSR of the rings. This means that the fabricated filter can be reconfigured at any frequency between DC and 31 GHz. To cover higher frequency bands, the filter can be redesigned with smaller rings (i.e. larger FSR). On the other hand, the bandwidth (BW) tunability of our proposed filter is shown in **Fig. 9** (bottom) for BW = 2.68, 3 and 3.69 GHz. A trade-off can be observed in **Fig. 9** (bottom), whereby as the BW is reduced, the passband insertion loss increases [52]. This becomes even more prominent when sub-GHz 3dB bandwidth settings are attempted. This is due to the losses in the rings, and can be mitigated by adopting low-loss multimode waveguide design [53] and/or utilizing the upcoming ultra low-loss PDK from AIM Photonics [25].

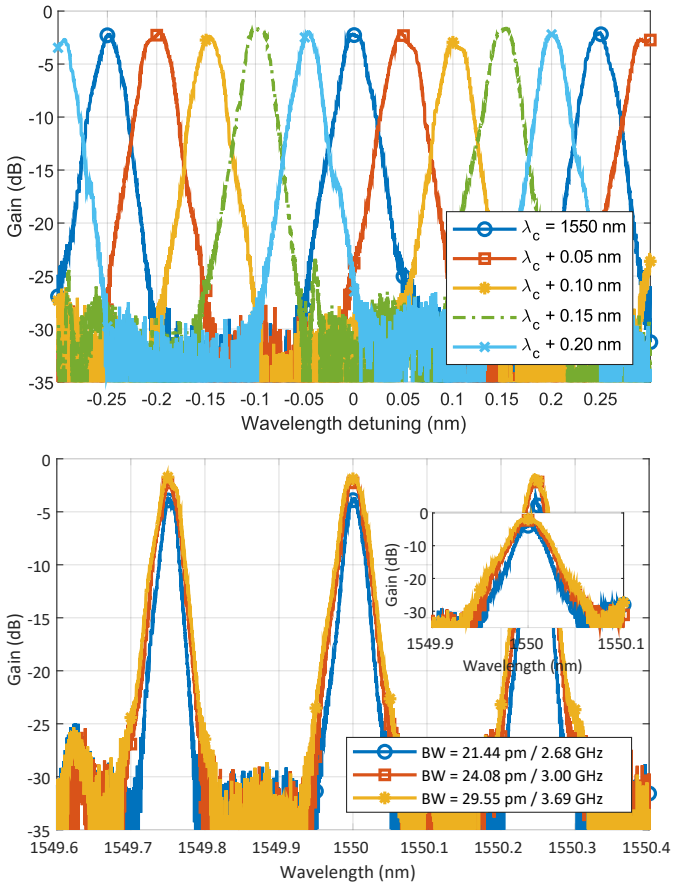

Fig. 9. (Top) Center frequency tuning of the silicon photonic filter. Here, the filter is configured at 5 different wavelengths with $\Delta\lambda = 0.05$ nm or $\Delta f = 6.25$ GHz. (bottom) Bandwidth Tuning of the filter around $\lambda_c = 1550$ nm.

In **Table III**, a comprehensive comparison of this work with other related work such as 2^{nd}-order APD filter [11], 4^{th}-order APD filter [11], 5^{th}-order CROW filter [14], 2^{nd}-order CROW filter [15], 4^{th}-order APD filter [52], Benes switch matrix based filter [54], filter based on phase-to-intensity modulation conversion [55] and higher order vernier filter [56] is provided. As evident from the comparison, this work presents a first fully-automatic filter tuning scheme with in-situ reconfiguration capability and a significant step towards a portable solution.

TABLE II
EXPLANATION OF DAC TUNING EVENTS.

Event	Details
A	Upper Ring coupler (UR-C) is set to zero coupling after a coarse and fine search.
B	Lower Ring coupler (LR-C) is set to zero coupling after a coarse and fine search.
C	Upper Ring coupler (UR-C) is set to desired coupling ratio based on **Algorithm 2**.
D	Lower Ring coupler (LR-C) is set to desired coupling ratio based on **Algorithm 2**.
E_n	n^{th} iteration of Upper Ring phase shifter (UR-PS) resonance alignment to λ_c after coarse and fine search.
F_n	n^{th} iteration of Lower Ring phase shifter (LR-PS) resonance alignment to λ_c after coarse and fine search.
G_n	n^{th} iteration of configuring Upper Ring phase shifter (UR-PS) phase bias ϕ_1 based on **Algorithm 4**.
H_n	n^{th} iteration of configuring Lower Ring phase shifter (LR-PS) phase bias ϕ_2 based on **Algorithm 4**.
I_n	n^{th} iteration of maximizing 10% monitor tap output by tuning Quadrature phase shifter (Q-PS).
J_n	n^{th} iteration of maximizing 10% monitor tap output by tuning Back-coupler (B-C).

VI. CONCLUSION AND FUTURE WORK

This work presented a robust silicon photonic filter for RF photonic applications with an improved reconfiguration algorithm that is insensitive to PVT variations. By utilizing the proposed in-situ configuration algorithm with simpler pre-characterization steps (i.e. without requiring an OVNA), we have experimentally shown that the filter can be configured to any desired center frequency, bandwidth, and rejection as per the user specifications with high fidelity. Moreover, the filter is the first of its class to be fabricated in AIM photonics's CMOS-compatible Active Photonic process, making the filter widely manufacturable at low cost for next-generation RF photonic systems. The proposed coupling coefficient extraction and configuration algorithm provides >2X improvement in configuration time over the prior art.

Further improvements such as sub-GHz bandwidth with low insertion loss can potentially be achieved by incorporating multimode & low-loss waveguide designs [53] and <1% monitor taps in the rings, and/or leveraging the planned ultra-low-loss PDK and MPW runs from AIM Photonics [25]. The current 2^{nd}-order filter initial reconfiguration time is around 725s. With our optimized algorithm and a low thermal crosstalk design where back-coupler and quadrature phase shifter tuning does not affect the ring bias (ϕ_n) as in [11], the filter reconfiguration time can be as fast as ∼300s. This can be achieved by careful planning of the PIC layout where the thermo-optic phase shifters (microheaters) are placed further

This article has been accepted for publication in IEEE/OSA Journal of Lightwave Technology. This is the author's version which has not been fully edited and content may change prior to final publication. Citation information: DOI 10.1109/JLT.2022.3222131
Accepted Manuscript
Version of record at: https://doi.org/10.1109/JLT.2022.3222131

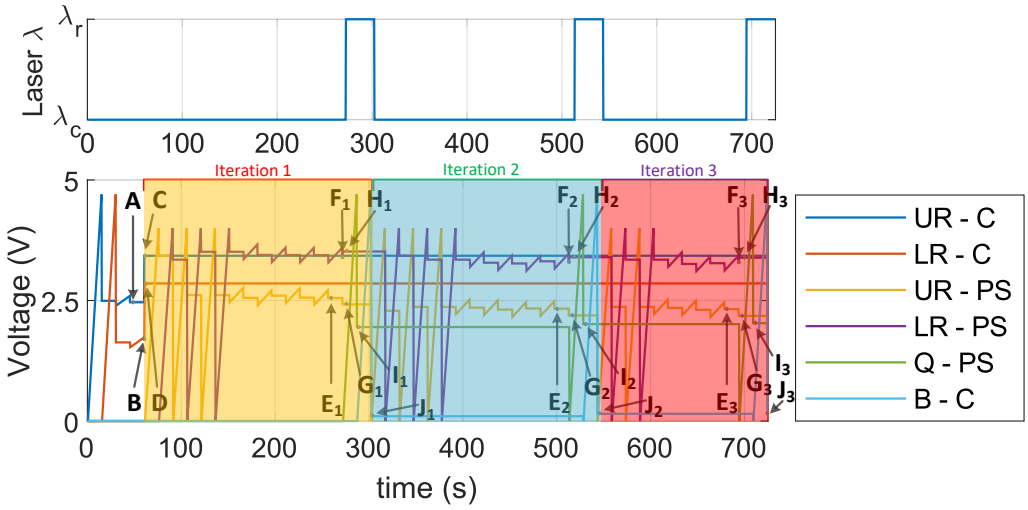

Fig. 8. DAC sampling and laser wavelength switching at different stages of silicon photonic filter reconfiguration. The corresponding timestamps are explained in detail in Table II. Each iteration corresponds to the ring phase, quadrature phase shifter, and back-coupler configuration steps. Here, three iterations were needed as the thermal crosstalk from the last back-coupler and quadrature phase shifter configuration step de-tunes the rings.

TABLE III
COMPARISON WITH STATE-OF-THE-ART IN FILTER TUNING.

Metric		This Work	Ref. [11]	Ref. [11]	Ref. [14]	Ref. [15]	Ref. [52]	Ref. [54]	Ref. [55]	Ref. [56]
Technology		AIM	IME SiP	IME SiP	IME SiP	IME SiP	BAE SiP	SiP	SiP	IME SiP
Architecture		APD	APD	APD	CROW	CROW	APD	Benes	PM-IM	Vernier
Order		2	2	4	5	2	4	2, 4	-	4
FSR (nm)		0.249 (31 GHz)	0.396 (50 GHz)	0.396 (50 GHz)	∼2.47 (308 GHz)	2.10 (265 GHz)	0.1307 (16.5 GHz)	8.3 (1.03 THz)	-	37.21 (4.64 THz)
BW (GHz)		3	6.89	5	∼30.9	33.4	1	∼46, ∼56	1.93	39
Rejection (dB)		30	32	33	∼50	25	25	16, 23.4	∼18	∼50
Passband Insertion Loss (dB)		2.2	∼2.3	4.67	∼2.64	2.11	6	10.3, 11.2	38.9	4.5
Reconfigurability	f_c	Y	Y	Y	Y	Y	Y	Y	Y	Y
	BW	Y	Y	Y	N	Y	Y	Y	N	N
	Rejection	Y	Y	Y	N	N	Y	N	N	N
Automatic Reconfiguration	f_c	Y	Y	Y	Y	Y	N	N	N	Y
	BW	Y	Y	Y	N	Y	N	N	N	N
	Rejection	Y	Y	Y	N	N	N	N	N	N
Portability		No OVNA	Uses OVNA	Uses OVNA	[2]NP	[2]NP	[1]NP	[1,2]NP	[1,2]NP	[2]NP

[1]NP = Not Portable. [2]NP = Lacks full configurability of all filter specifications.

apart from sensitive waveguides (rings) at the expense of a larger footprint.

Achieving rapid filter reconfiguration on the order of seconds in frequency-agile SDRs will require even higher thermal isolation between on-chip photonic components. This can potentially be achieved by the integration of microheaters with undercut [51] in a SiP foundry process. Recent early results with undercut-based thermo-optic heaters have exhibited promising performance with a $P_\pi \sim 1.2$ mW [57], which is over 25X reduction, and the resulting thermal isolation is expected to significantly reduce thermal crosstalk. The challenges associated with alternative optical tuning methods such as Brillouin scattering and optical MEMS in silicon have been discussed earlier, and improvements in thermo-optic tuning is expected to enable rapid filter tuning over the alternatives.

In summary, by taking full advantage of the large-volume low-cost manufacturing of a CMOS-compatible photonic process, the presented RF photonic filters and improved reconfiguration algorithm provide a way forward for wider adoption in high-performance RF and microwave photonic transceivers.

VII. ACKNOWLEDGMENT

The authors gratefully acknowledge the generous funding support from the Air Force Office of Sponsored Research (AFOSR) YIP Award FA9550-17-1-0076, DARPA YFA Award HR00112110001, and the National Science Foundation (NSF) CAREER Award EECS-2014109. The authors also thank AIM Photonics and gratefully acknowledge APSUNY PDK Component Library.

REFERENCES

[1] J. Capmany, G. Li, C. Lim, and J. Yao, "Microwave photonics: current challenges towards widespread application," *Optics express*, vol. 21, no. 19, pp. 22 862–22 867, 2013.
[2] V. J. Urick, K. J. Williams, and J. D. McKinney, *Fundamentals of microwave photonics*. John Wiley & Sons, 2015.
[3] X. Yi, S. X. Chew, S. Song, L. Nguyen, and R. Minasian, "Integrated microwave photonics for wideband signal processing," in *Photonics*, vol. 4. Multidisciplinary Digital Publishing Institute, 2017, p. 46.

[4] R. A. Minasian, E. Chan, and X. Yi, "Microwave photonic signal processing," *Optics Express*, vol. 21, no. 19, pp. 22 918–22 936, 2013.
[5] D. Marpaung, C. Roeloffzen, R. Heideman, A. Leinse, S. Sales, and J. Capmany, "Integrated microwave photonics," *Laser & Photonics Reviews*, vol. 7, no. 4, pp. 506–538, 2013.
[6] W. Zhang and J. Yao, "Silicon-based integrated microwave photonics," *IEEE Journal of Quantum Electronics*, vol. 52, no. 1, pp. 1–12, 2015.
[7] D. Sadot and E. Boimovich, "Tunable optical filters for dense wdm networks," *IEEE Communications Magazine*, vol. 36, no. 12, pp. 50–55, 1998.
[8] R. Baets, A. Z. Subramanian, A. Dhakal, S. K. Selvaraja, K. Komorowska, F. Peyskens, E. Ryckeboer, N. Yebo, G. Roelkens, and N. Le Thomas, "Spectroscopy-on-chip applications of silicon photonics," in *Integrated optics: Devices, materials, and technologies XVII*, vol. 8627. Spie, 2013, pp. 87–96.
[9] S. Gringeri, B. Basch, V. Shukla, R. Egorov, and T. J. Xia, "Flexible architectures for optical transport nodes and networks," *IEEE Communications Magazine*, vol. 48, no. 7, pp. 40–50, 2010.
[10] J. M. F. Cabanillas, D. Kramnik, A. Ramesh, C. M. Gentry, V. Stojanović, P. Kumar, and M. A. Popović, "Tunable source of quantum-correlated photons with integrated pump rejection in a silicon cmos platform," in *Frontiers in Optics*. Optical Society of America, 2021, pp. FTu2E–1.
[11] G. Choo, S. Cai, B. Wang, C. K. Madsen, K. Entesari, and S. Palermo, "Automatic Monitor-Based Tuning of Reconfigurable Silicon Photonic APF-Based Pole/Zero Filters," *Journal of Lightwave Technology*, vol. 36, no. 10, pp. 1899–1911, 2018.
[12] R. Won, "Integrating silicon photonics," *Nature photonics*, vol. 4, no. 8, pp. 498–499, 2010.
[13] W. Bogaerts and L. Chrostowski, "Silicon photonics circuit design: methods, tools and challenges," *Laser & Photonics Reviews*, vol. 12, no. 4, p. 1700237, 2018.
[14] J. C. Mak, W. D. Sacher, T. Xue, J. C. Mikkelsen, Z. Yong, and J. K. Poon, "Automatic resonance alignment of high-order microring filters," *IEEE Journal of Quantum Electronics*, vol. 51, no. 11, pp. 1–11, 2015.
[15] J. C. Mak, A. Bois, and J. K. Poon, "Programmable multiring butterworth filters with automated resonance and coupling tuning," *IEEE Journal of Selected Topics in Quantum Electronics*, vol. 22, no. 6, pp. 232–240, 2016.
[16] S. Liao, Y. Ding, C. Peucheret, T. Yang, J. Dong, and X. Zhang, "Integrated programmable photonic filter on the silicon-on-insulator platform," *Optics Express*, vol. 22, no. 26, pp. 31 993–31 998, 2014.
[17] J. Kim, W. J. Sung, O. Eknoyan, and C. K. Madsen, "Linear photonic frequency discriminator on as 2 s 3-ring-on-ti: Linbo 3 hybrid platform," *Optics Express*, vol. 21, no. 21, pp. 24 566–24 573, 2013.
[18] J. Kim, D. B. Adams, and C. K. Madsen, "Device-under-test jones matrix extraction algorithm with device te/tm reference frame," *IEEE Photonics Technology Letters*, vol. 24, no. 1, pp. 88–90, 2011.
[19] V. Saxena, "PICTorch: Photonic Integrated Circuit Simulator," 2022. [Online]. Available: https://github.com/AMPIC/PICTorch
[20] J. Capmany and D. Pérez, *Programmable Integrated Photonics*. Oxford University Press, 2020.
[21] "AP SUNY Component Library." [Online]. Available: https://www.aimphotonics.com/apsuny-component-library
[22] N. M. Fahrenkopf, C. McDonough, G. L. Leake, Z. Su, E. Timurdogan, and D. D. Coolbaugh, "The aim photonics mpw: A highly accessible cutting edge technology for rapid prototyping of photonic integrated circuits," *IEEE Journal of Selected Topics in Quantum Electronics*, vol. 25, no. 5, pp. 1–6, 2019.
[23] P. A. Regalia, S. K. Mitra, and P. Vaidyanathan, "The digital all-pass filter: A versatile signal processing building block," *Proceedings of the IEEE*, vol. 76, no. 1, pp. 19–37, 1988.
[24] C. Madsen, "Efficient architectures for exactly realizing optical filters with optimum bandpass designs," *Photonics Technology Letters, IEEE*, vol. 10, no. 8, pp. 1136–1138, 1998.
[25] "Aim photonics, url: http://www.aimphotonics.com/pdk/." [Online]. Available: http://www.aimphotonics.com/pdk/
[26] M. R. Watts, J. Sun, C. DeRose, D. C. Trotter, R. W. Young, and G. N. Nielson, "Adiabatic thermo-optic mach–zehnder switch," *Optics letters*, vol. 38, no. 5, pp. 733–735, 2013.
[27] Ansys, "Lumerical interconnect." [Online]. Available: https://www.lumerical.com/products/interconnect/
[28] F. Laporte, J. Dambre, and P. Bienstman, "Highly parallel simulation and optimization of photonic circuits in time and frequency domain based on the deep-learning framework pytorch," *Scientific reports*, vol. 9, no. 1, pp. 1–9, 2019.
[29] C. Li, K. Yu, J. Rhim, K. Zhu, N. Qi, M. Fiorentino, T. Pinguet, M. Peterson, V. Saxena, and S. Palermo, "A 3d-integrated 56 gb/s nrz/pam4 reconfigurable segmented mach-zehnder modulator-based si-photonics transmitter," in *2018 IEEE BiCMOS and Compound Semiconductor Integrated Circuits and Technology Symposium (BCICTS)*. IEEE, 2018, pp. 32–35.
[30] K. Zhu, V. Saxena, X. Wu, and W. Kuang, "Design considerations for traveling-wave modulator-based cmos photonic transmitters," *IEEE Transactions on Circuits and Systems II: Express Briefs*, vol. 62, no. 4, pp. 412–416, 2015.
[31] N. Pavarelli, J. S. Lee, M. Rensing, C. Scarcella, S. Zhou, P. Ossieur, and P. A. O'Brien, "Optical and electronic packaging processes for silicon photonic systems," *Journal of Lightwave Technology*, vol. 33, no. 5, pp. 991–997, 2015.
[32] "Photonic packaging." [Online]. Available: https://www.tyndall.ie/packaging/
[33] A. Malik, C. Xiang, L. Chang, W. Jin, J. Guo, M. Tran, and J. Bowers, "Low noise, tunable silicon photonic lasers," *Applied Physics Reviews*, vol. 8, no. 3, p. 031306, 2021.
[34] "Fp3015c c-band tunable laser." [Online]. Available: https://freedomphotonics.com/freedom-photonics-products/lasers-and-laser-systems/1550-nm-c-band-tunable-laser-fp3015c
[35] *EasySMU: I2C Address Translator and Simple Multichannel Source Measurement Unit*, Analog Devices, 2021. [Online]. Available: https://www.analog.com/en/design-center/evaluation-hardware-and-software/evaluation-boards-kits/dc2591a.html
[36] L. Chrostowski and M. Hochberg, *Silicon Photonics Design: From Devices to Systems*. Cambridge University Press, 2015.
[37] G. T. Reed, G. Mashanovich, F. Gardes, and D. Thomson, "Silicon optical modulators," *Nature photonics*, vol. 4, no. 8, pp. 518–526, 2010.
[38] C. G. Bottenfield, V. A. Thomas, and S. E. Ralph, "Silicon photonic modulator linearity and optimization for microwave photonic links," *IEEE Journal of Selected Topics in Quantum Electronics*, vol. 25, no. 5, pp. 1–10, 2019.
[39] B. J. Eggleton, C. G. Poulton, P. T. Rakich, M. Steel, G. Bahl *et al.*, "Brillouin integrated photonics," *Nature Photonics*, vol. 13, no. 10, pp. 664–677, 2019.
[40] D. Marpaung, M. Pagani, B. Morrison, and B. J. Eggleton, "Nonlinear integrated microwave photonics," *Journal of Lightwave Technology*, vol. 32, no. 20, pp. 3421–3427, 2014.
[41] Y. Liu, A. Choudhary, G. Ren, K. Vu, B. Morrison, A. Casas-Bedoya, T. G. Nguyen, D.-Y. Choi, P. Ma, A. Mitchell *et al.*, "Integration of brillouin and passive circuits for enhanced radio-frequency photonic filtering," *APL Photonics*, vol. 4, no. 10, p. 106103, 2019.
[42] N. Quack, H. Sattari, A. Y. Takabayashi, Y. Zhang, P. Verheyen, W. Bogaerts, P. Edinger, C. Errando-Herranz, and K. B. Gylfason, "Mems-enabled silicon photonic integrated devices and circuits," *IEEE Journal of Quantum Electronics*, vol. 56, no. 1, pp. 1–10, 2019.
[43] W. Bogaerts, H. Sattari, P. Edinger, A. Y. Takabayashi, I. Zand, X. Wang, A. Ribeiro, M. Jezzini, C. Errando-Herranz, G. Talli *et al.*, "Morphic: programmable photonic circuits enabled by silicon photonic mems," in *Silicon Photonics XV*, vol. 11285. SPIE, 2020, p. 1128503.
[44] R. Helkey, A. A. Saleh, J. Buckwalter, and J. E. Bowers, "High-performance photonic integrated circuits on silicon," *IEEE Journal of Selected Topics in Quantum Electronics*, vol. 25, no. 5, pp. 1–15, 2019.
[45] W. Jin, R. G. Polcawich, P. A. Morton, and J. E. Bowers, "Piezoelectrically tuned silicon nitride ring resonator," *Optics Express*, vol. 26, no. 3, pp. 3174–3187, 2018.
[46] W. Bogaerts, P. De Heyn, T. Van Vaerenbergh, K. De Vos, S. Kumar Selvaraja, T. Claes, P. Dumon, P. Bienstman, D. Van Thourhout, and R. Baets, "Silicon microring resonators," *Laser & Photonics Reviews*, vol. 6, no. 1, pp. 47–73, 2012.
[47] H. Li, G. Balamurugan, M. Sakib, R. Kumar, H. Jayatilleka, H. Rong, J. Jaussi, and B. Casper, "12.1 a 3d-integrated microring-based 112gb/s pam-4 silicon-photonic transmitter with integrated nonlinear equalization and thermal control," in *2020 IEEE International Solid-State Circuits Conference-(ISSCC)*. IEEE, 2020, pp. 208–210.
[48] M. J. Shawon and V. Saxena, "Rapid simulation of photonic integrated circuits using verilog-a compact models," in *2019 IEEE 62nd International Midwest Symposium on Circuits and Systems (MWSCAS)*. IEEE, 2019, pp. 424–427.
[49] ——, "Rapid simulation of photonic integrated circuits using verilog-a compact models," *IEEE Transactions on Circuits and Systems I: Regular Papers*, vol. 67, no. 10, pp. 3331–3341, 2020.
[50] A. Masood, M. Pantouvaki, G. Lepage, P. Verheyen, J. Van Campenhout, P. Absil, D. Van Thourhout, and W. Bogaerts, "Comparison of heater

architecture for thermal control of silicon photonics circuits," in *IEEE Group IV Photonics*, 2013, pp. 83–84.

[51] D. Coenen, H. Oprins, Y. Ban, F. Ferraro, M. Pantouvaki, J. Van Campenhout, and I. De Wolf, "Thermal modelling of silicon photonic ring modulator with substrate undercut," *Journal of Lightwave Technology*, 2022.

[52] M. S. Rasras, D. M. Gill, S. S. Patel, K.-Y. Tu, Y.-K. Chen, A. E. White, A. T. Pomerene, D. N. Carothers, M. J. Grove, D. K. Sparacin, J. Michel, M. A. Beals, and L. C. Kimerling, "Demonstration of a fourth-order pole-zero optical filter integrated using CMOS processes," *Journal of Lightwave Technology*, vol. 25, no. 1, pp. 87–92, 2007.

[53] D. Onural, H. Gevorgyan, B. Zhang, A. Khilo, and M. A. Popović, "Ultra-high q resonators and sub-ghz bandwidth second order filters in an soi foundry platform," in *Optical Fiber Communication Conference*. Optical Society of America, 2020, pp. W1A–4.

[54] L. Shen, L. Lu, Z. Guo, L. Zhou, and J. Chen, "Silicon optical filters reconfigured from a 16× 16 benes switch matrix," *Optics Express*, vol. 27, no. 12, pp. 16 945–16 957, 2019.

[55] W. Zhang and J. Yao, "On-chip silicon photonic integrated frequency-tunable bandpass microwave photonic filter," *Optics Letters*, vol. 43, no. 15, pp. 3622–3625, 2018.

[56] H. Jayatilleka, R. Boeck, M. AlTaha, J. Flueckiger, N. A. Jaeger, S. Shekhar, and L. Chrostowski, "Automatic tuning and temperature stabilization of high-order silicon vernier microring filters," in *Optical Fiber Communication Conference*. Optical Society of America, 2017, pp. Th1G–4.

[57] A. Rizzo, S. Daudlin, A. Novick, A. James, V. Gopal, V. Murthy, Q. Cheng, B. Y. Kim, X. Ji, Y. Okawachi *et al.*, "Petabit-scale silicon photonic interconnects with integrated kerr frequency combs," *IEEE Journal of Selected Topics in Quantum Electronics*, vol. 29, no. 1: Nonlinear Integrated Photonics, pp. 1–20, 2022.

Md Jubayer Shawon (Student Member, IEEE) is a Ph.D. candidate in the Department of Electrical and Computer Engineering at the University of Delaware, DE. His research includes the development of Large-scale Programmable & Reconfigurable RF Photonic Integrated circuits that combine CMOS and Silicon Photonic ICs for RF/millimeter-wave applications, and Optical Interconnects. He has also worked on CMOS RF MEMS devices with the Technology Development group of SilTerra Semiconductor foundry, Malaysia. Additionally, he also worked at IMEC, Belgium on developing control electronics for Smart Photovoltaic arrays. He received his B.Sc. degree in Electrical & Electronic Engineering from Bangladesh University of Engineering & Technology in 2013, M.Eng.Sc. degree in Photonics from the University of Malaya, Malaysia in 2016 and Masters in Electrical Engineering from the University of Idaho, ID in 2019.

Vishal Saxena (Senior Member, IEEE) is an Associate Professor in Electrical and Computer Engineering at the University of Delaware, where he directs the Analog Mixed-Signal and Photonic Integrated Circuits (AMPIC) lab. He obtained his B. Tech. Degree in Electrical Engineering from the Indian Institute of Technology, Madras, in 2002 and M.S. and Ph.D. from Boise State University, ID, in 2007 and 2010, respectively. Dr. Saxena is a recipient of the 2015 NSF CAREER, the 2016 AFOSR Young Investigator Program (YIP), and the 2019 DARPA Young Faculty Award (YFA) awards. He is a Senior Member of IEEE. He currently serves as an Associate Editor for IEEE TCAS-II journal and on the steering committee of the IEEE MWSCAS conference and ISCAS VLSI Committee. His research interests include CMOS photonic interconnects, RF and millimeter-wave Photonic ICs, Neuromorphic, Edge-AI, and Quantum computing.